molecules

MDPI

Article

Phase Separation Phenomena in Lightly Cu-Doped A-Site-Ordered Quadruple Perovskite $NdMn_7O_{12}$

Alexei A. Belik [1,*], Ran Liu [1,2,3] and Kazunari Yamaura [1,2]

[1] Research Center for Materials Nanoarchitectonics (MANA), National Institute for Materials Science (NIMS), Namiki 1-1, Tsukuba 305-0044, Ibaraki, Japan; liu.ran@sanken.osaka-u.ac.jp (R.L.); yamaura.kazunari@nims.go.jp (K.Y.)
[2] Graduate School of Chemical Sciences and Engineering, Hokkaido University, North 10 West 8, Kita-ku, Sapporo 060-0810, Hokkaido, Japan
[3] Institute of Scientific and Industrial Research, Osaka University, Mihogaoka 8-1, Ibaraki 567-0047, Osaka, Japan
* Correspondence: alexei.belik@nims.go.jp

Abstract

A-site-ordered quadruple perovskite manganites, AMn_7O_{12}, show many interesting physical phenomena, including orbital and spin modulations, spin-induced multiferroic properties, and competitions between different magnetic ground states. Doping with Cu^{2+} can result in colossal magnetoresistance properties, ferrimagnetism, and additional structural modulations producing electric–dipole helicoidal textures. Many previous works have focused on large-concentration doping, reaching $ACu_3Mn_4O_{12}$ compositions. Small-concentration doping has been investigated in a limited number of systems, e.g., in $BiCu_xMn_{7-x}O_{12}$. In this work, we investigated solid solutions of $NdCu_xMn_{7-x}O_{12}$ with x = 0.1, 0.2, and 0.3, prepared at 6 GPa and 1500 K. Specific heat measurements detected three magnetic transitions at x = 0 (at T_{N3} = 9 K, T_{N2} = 12 K, and T_{N1} = 84 K) and two transitions at x = 0.1 (at T_{N2} = 10 K and T_{N1} = 78 K), while only one transition was found at x = 0.2 (T_{N1} = 72 K) and x = 0.3 (T_{N1} = 65 K). Differential scanning calorimetry (DSC) measurements showed sharp and strong peaks near T_{OO} = 664 K at x = 0, corresponding to an orbital-order (OO) structural transition from $I2/m$ to Im-3 symmetry. DSC anomalies were significantly broadened and their intensities were significantly reduced at x = 0.1–0.3, and structural transitions were observed near T_{OO} = 630 K at x = 0.1, T_{OO} = 600 K at x = 0.2, and T_{OO} = 570 K at x = 0.3. The x = 0.1 sample clearly showed double-peak features on the DSC curves near T_{OO} because of the presence of two close phases. High-resolution synchrotron powder X-ray diffraction studies gave strong evidence that phase separation phenomena took place in the x = 0.1–0.3 samples, where two $I2/m$ phases with an approximate ratio of 1:1 were present (e.g., a = 7.47143 Å, b = 7.36828 Å, c = 7.46210 Å, and β = 90.9929° for one phase and a = 7.46596 Å, b = 7.37257 Å, c = 7.45756 Å, and β = 90.9328° for the second phase at x = 0.3). The Curie–Weiss temperature changed from negative (for x = 0, 0.1, and 0.2) to positive (for x = 0.3). T_{OO}, T_{N1}, the Curie–Weiss temperature, and magnetization (at 5 K and 70 kOe) changed almost linearly with x.

Keywords: A-site-ordered quadruple perovskites; orbital order; phase separation

Academic Editor: Takashiro Akitsu

Received: 29 October 2025
Revised: 21 November 2025
Accepted: 25 November 2025
Published: 26 November 2025

Citation: Belik, A.A.; Liu, R.; Yamaura, K. Phase Separation Phenomena in Lightly Cu-Doped A-Site-Ordered Quadruple Perovskite $NdMn_7O_{12}$. *Molecules* **2025**, *30*, 4561. https://doi.org/10.3390/molecules30234561

1. Introduction

Classical perovskite-structure materials with the stoichiometry of ABO_3 have large A cations and smaller B cations [1–5]. The stability of the perovskite structure is de-

termined by the relative sizes of A and B cations and is usually understood in terms of the Goldschmidt tolerance factor [2]. The perovskite structure (at least, in the oxide form) is quite flexible and can adapt (and form ordered structures) to situations where some A cations (defined as A′ and A″) have similar sizes to B cations. Such adaptations take place through the $a^+a^+a^+$ tilt (in Glazer's notation [6]) in the case of A-site-ordered quadruple perovskites, $AA'_3B_4O_{12}$ [7–13], and through the $a^+a^+c^-$ tilt in the case of A-site columnar-ordered quadruple perovskites, $A_2A'A''B_4O_{12}$ [13]. Strong octahedral tilting produces square planar coordination (as the first coordination sphere) around the A′ sites in both subfamilies.

If A′ = B = Mn in A-site-ordered quadruple $AA'_3B_4O_{12}$ perovskites, an interesting class of perovskite manganites is formed, $AMn_3Mn_4O_{12}$ or AMn_7O_{12} in short form [12]. Depending on the oxidation state of the A cation, Mn cations can take different oxidation states (at the B sites) from +3.5 for A^+ [14,15] to +3.25 for A^{2+} [16] to +3 for A^{3+} [17–34], while Mn cations usually take the +3 oxidation state at the A′ site. The average oxidation state of Mn at the B sites determines the structural and magnetic behaviors of AMn_7O_{12}. All AMn_7O_{12} compounds crystallize in the parent structure of the $AA'_3B_4O_{12}$ quadruple perovskites with space group *Im*-3 at high temperatures. However, with decreasing temperature, different structural distortions take place. For example, all members of the trivalent subfamily $A^{3+}Mn_7O_{12}$ (except $BiMn_7O_{12}$ [20–22]) crystallize in the monoclinic space group *I*2/*m* at room temperature (RT). The *Im*-3 to *I*2/*m* transition is driven by the orbital ordering (OO) of Jahn–Teller active Mn^{3+} cations at the B sites.

The average oxidation state of Mn at the B sites can be continuously changed in different solid solutions, such as $A^+Mn_7O_{12}$–$A^{2+}Mn_7O_{12}$ and $A^{2+}Mn_7O_{12}$–$A^{3+}Mn_7O_{12}$ [35–37]. The average oxidation state of Mn at the B sites can also be controlled through Cu^{2+} doping, producing $ACu_xMn_{7-x}O_{12}$ solid solutions. Cu^{2+} cations are usually selected as dopants because Cu^{2+} cations occupy square planar sites similar to Mn^{3+} cations and do not disturb/dilute Mn in the B sublattice [38–55]. With Cu^{2+} doping, the Mn^{3+}/Mn^{4+} ratio is only changed in the B sublattice. Large Cu^{2+} doping, e.g., reaching $ACu_3Mn_4O_{12}$ [46–55], produces ferrimagnetic (FiM) properties with high magnetic transition temperatures above RT. Such $A^{2+}Mn_7O_{12}$ and $A^{3+}Mn_7O_{12}$ manganites also show good catalytic properties [10].

It was recently found that light Cu^{2+} doping of $BiMn_7O_{12}$ can introduce electric-dipole helicoidal textures [56], mesoscopic helices of polar domains [57], and complex temperature–composition phase diagrams [58,59]. Light Cu^{2+} doping of other members of the trivalent subfamily $A^{3+}Mn_7O_{12}$ has been poorly investigated. $LaCu_xMn_{7-x}O_{12}$ solid solutions were only studied at small doping levels [60]. However, the structural evolution at RT was only reported as a function of x without detailed physical properties [60]. It was found that the monoclinic *I*2/*m* structure of the parent $LaMn_7O_{12}$ was realized at x = 0.12–0.32, the *R*-3 structure, observed in $Ca^{2+}Mn_7O_{12}$ [16], was realized at x = 0.52–0.84, and the cubic *Im*-3 parent structure of $AA'_3B_4O_{12}$ quadruple perovskites was realized at x = 1–3 [60]. Detailed effects of the low doping levels of Cu^{2+} were mainly investigated in $CaMn_7O_{12}$ [61–65], where incommensurate crystal and magnetic structures are highly sensitive to such doping. We emphasize that previous structural studies with neutron diffraction [44,51,53,56,58,59,61] showed that Cu^{2+} cations are always localized at the square planar A′ site due to the strong Jahn–Teller effect of Cu^{2+}.

Therefore, in this work, we prepared and investigated $NdCu_xMn_{7-x}O_{12}$ solid solutions at small doping levels of x = 0.1, 0.2, and 0.3. We found that the $NdCu_xMn_{7-x}O_{12}$ solid solutions preserve the monoclinic structure of the parent $NdMn_7O_{12}$. However, the phase separation phenomenon was observed, where two close monoclinic *I*2/*m* phases were present in $NdCu_xMn_{7-x}O_{12}$ solid solutions. The structural divergence between the two phases monotonically increases with increasing x. The Curie–Weiss temperature

changes from negative (for x = 0, 0.1, and 0.2) to positive (for x = 0.3). The structural transition temperature ($T_{str} = T_{OO}$), the first magnetic transition temperature (T_{N1}), the Curie–Weiss temperature, and magnetization (at 5 K and 70 kOe) change almost linearly with x.

2. Results and Discussion

2.1. Magnetic Properties

The χ versus T curves of $NdMn_7O_{12}$ clearly showed three magnetic anomalies (Figure 1) at T_{N3} = 9 K, T_{N2} = 12 K, and T_{N1} = 84 K [33,34]. A transition at T_{N1} = 84 K shows sharp increases in the χ values (especially at H = 100 Oe). Then, there are additional small increases in the χ values at T_{N2} = 12 K and H = 10 kOe and small drops in the χ values at T_{N3} = 9 K and H = 10 kOe. The behavior of the χ versus T curves of $NdMn_7O_{12}$ at H = 10 kOe agrees well with magnetic structures found by neutron diffraction studies [33]. Below T_{N1}, a FiM transition takes place on the Mn sublattice at the A′ site (with one Mn^{3+} uncompensated moment per unit cell), while an antiferromagnetic (AFM) order is realized on the Mn sublattice at the B site. The presence of one uncompensated site leads to a strong rise in χ values below T_{N1}. Below T_{N2}, small spin canting of the AFM spins and incommensurate spin modulation appear at the B site—this leads to an additional small increase in χ values below T_{N2}. Below T_{N3}, the Nd^{3+} sublattice is ordered with moments being antiparallel to the FiM moments of Mn^{3+} at the A′ site—this leads to small drops in χ values at T_{N3} = 9 K.

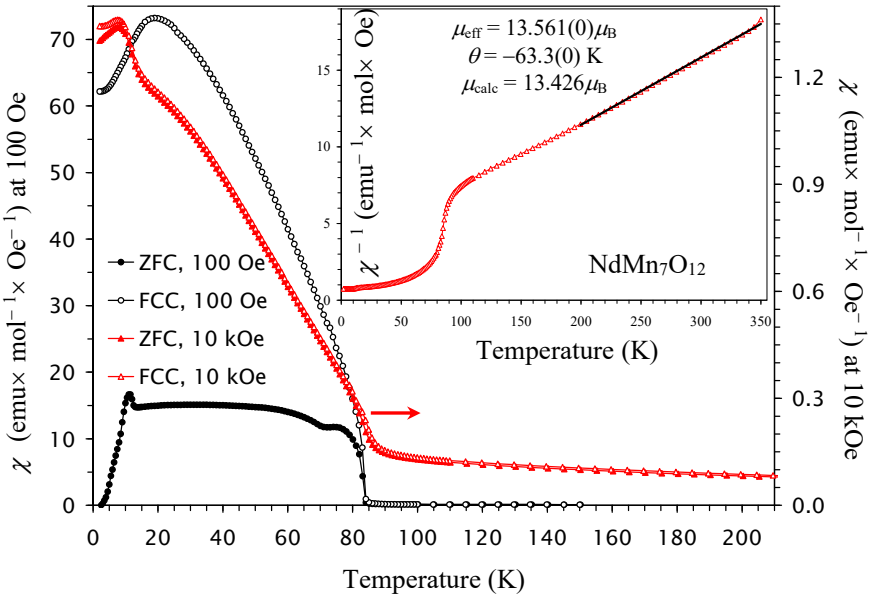

Figure 1. ZFC (filled symbols) and FCC (empty symbols) dc magnetic susceptibility curves ($\chi = M/H$) of $NdMn_7O_{12}$ measured at H = 100 Oe (black symbols; the left-hand axis) and H = 10 kOe (red symbols; the right-hand axis). The inset shows the 10 kOe FCC χ^{-1} versus T curve with the Curie–Weiss fit (black line) between 200 K and 350 K; the parameters of the fit (μ_{eff} and θ) are given in the figure.

The χ versus T curves of $NdCu_{0.1}Mn_{6.9}O_{12}$ (Figure 2) showed the first strong increases in the χ values below T_{N1} = 78 K. However, the additional upturn (observed near 12 K in $NdMn_7O_{12}$) nearly disappeared, while the small drops survived (near 10 K). Therefore, we can suggest that an incommensurate ordering (observed below T_{N2} = 12 K in $NdMn_7O_{12}$) is suppressed, and only magnetic transitions, corresponding to T_{N1} and T_{N3} in $NdMn_7O_{12}$, survived. The Nd sublattice remained undisturbed; therefore, the Nd sublattice can behave similarly in $NdMn_7O_{12}$ and $NdCu_{0.1}Mn_{6.9}O_{12}$. Cu^{2+} cations should be

located at the A′ sites; however, Cu^{2+} doping introduces Mn^{4+} cations at the B sites of $NdCu_{0.1}Mn_{6.9}O_{12}$. Therefore, the incommensurate ordering and spin canting at the B sites could be strongly affected by Cu^{2+} doping. In comparison with $NdMn_7O_{12}$, T_{N2} disappears in $NdCu_{0.1}Mn_{6.9}O_{12}$. However, we use sequential numbering of magnetic phase transitions with T_{N2} = 10 K and T_{N1} = 78 K for $NdCu_{0.1}Mn_{6.9}O_{12}$.

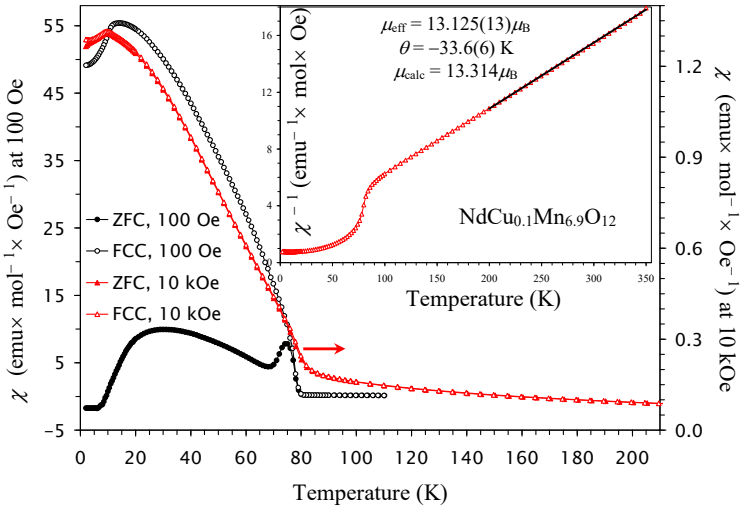

Figure 2. ZFC (filled symbols) and FCC (empty symbols) dc magnetic susceptibility curves ($\chi = M/H$) of $NdCu_{0.1}Mn_{6.9}O_{12}$ measured at H = 100 Oe (black symbols; the left-hand axis) and H = 10 kOe (red symbols; the right-hand axis). The inset shows the 10 kOe FCC χ^{-1} versus T curve with the Curie–Weiss fit (black line) between 200 K and 350 K; the parameters of the fit (μ_{eff} and θ) are given in the figure.

The low-temperature drops are further suppressed in $NdCu_{0.2}Mn_{6.8}O_{12}$ (Figure 3) and completely disappear in $NdCu_{0.3}Mn_{6.7}O_{12}$ in all magnetic fields (Figure 4). The transition temperatures are summarized in Table 1, and the first transition temperature (T_{N1}) almost linearly decreases with increasing x in the $NdCu_xMn_{7-x}O_{12}$ solid solutions (Figure 5a).

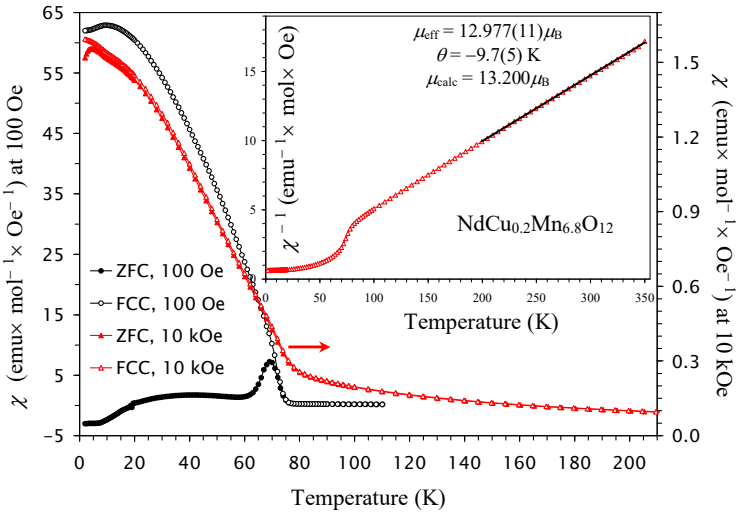

Figure 3. ZFC (filled symbols) and FCC (empty symbols) dc magnetic susceptibility curves ($\chi = M/H$) of $NdCu_{0.2}Mn_{6.8}O_{12}$ measured at H = 100 Oe (black symbols; the left-hand axis) and H = 10 kOe (red symbols; the right-hand axis). The inset shows the 10 kOe FCC χ^{-1} versus T curve with the Curie–Weiss fit (black line) between 200 K and 350 K; the parameters of the fit (μ_{eff} and θ) are given in the figure.

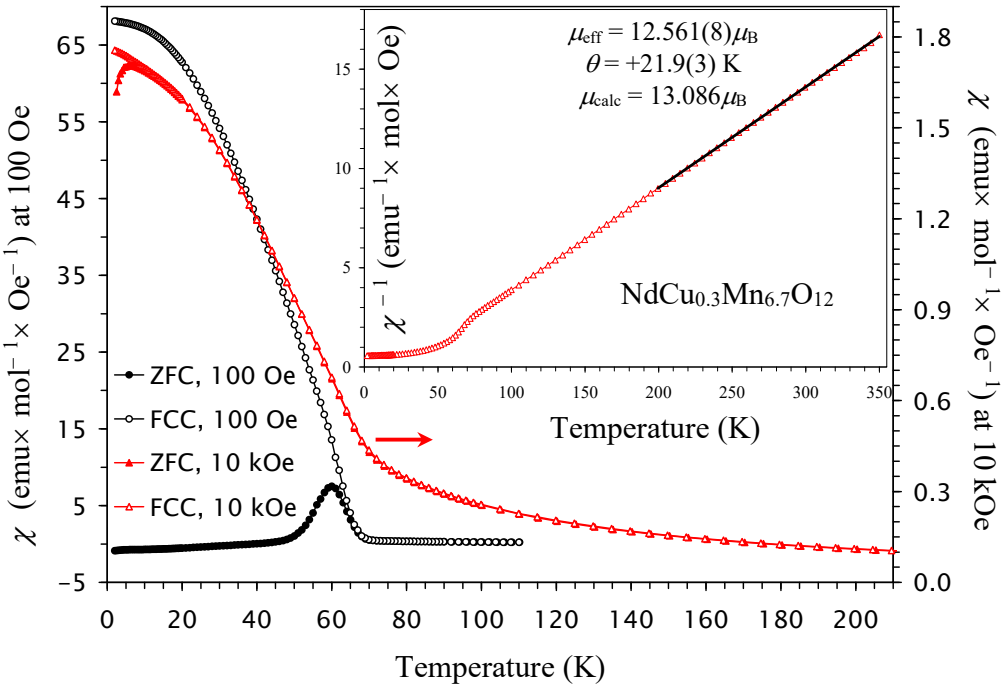

Figure 4. ZFC (filled symbols) and FCC (empty symbols) dc magnetic susceptibility curves ($\chi = M/H$) of $NdCu_{0.3}Mn_{6.7}O_{12}$ measured at H = 100 Oe (black symbols; the left-hand axis) and H = 10 kOe (red symbols; the right-hand axis). The inset shows the 10 kOe FCC χ^{-1} versus T curve with the Curie–Weiss fit (black line) between 200 K and 350 K; the parameters of the fit (μ_{eff} and θ) are given in the figure.

Table 1. Temperatures of structural transitions (T_{str}) and magnetic anomalies (T_N) and parameters of the Curie–Weiss fits and M versus H curves at T = 5 K for $NdCu_xMn_{7-x}O_{12}$ with x = 0, 0.1, 0.2, and 0.3.

x	T_{str} (K)	T_N (K)	μ_{eff} (μ_B/f.u.)	μ_{calc} (μ_B/f.u.)	θ (K)	M_S (μ_B/f.u.)	M_R (μ_B/f.u.)	H_C (kOe/f.u.)
0	664	9, 12, 84	13.651	13.426	−63.3	4.74	1.04	~0.4
0.1	~630	10, 78	13.125	13.314	−33.6	5.78	1.19	~1.0
0.2	~600	72	12.977	13.200	−9.7	6.64	1.53	~1.5
0.3	~570	65	12.561	13.086	+21.9	7.58	1.64	~3.3

The Curie–Weiss fits were performed between 200 and 350 K using the FCC χ^{-1} versus T data at 10 kOe. M_S is the magnetization value at T = 5 K and H = 70 kOe. M_R is the remnant magnetization value at T = 5 K. H_C is the coercive field at T = 5 K. μ_{eff} is an experimental effective magnetic moment. μ_{calc} is a calculated effective magnetic moment based on the formal oxidation states. T_N values were determined from peaks on the 100 Oe and 10 kOe FCC $d(\chi T)/dT$ versus T curves. T_{str} values were determined from peak positions on the heating (or cooling for x = 0.3) DSC curves. T_{str} corresponds to a transition to the *Im*-3 modification.

At high temperatures, the inverse magnetic susceptibilities followed the Curie–Weiss law. To extract the Curie–Weiss parameters, we fitted the field-cooled inverse magnetic susceptibilities (at H = 10 kOe) between 200 K and 350 K. The fitting parameters are summarized in Table 1 [66]. The Curie–Weiss temperature changes from negative (for x = 0, 0.1, and 0.2) to positive (for x = 0.3), and it follows a nearly linear change with x (Figure 5b). The increase in Cu^{2+} doping increases the concentration of Mn^{4+} at the B sites. Therefore, the concentration of ferromagnetic (FM) interactions through the double-exchange mechanism between Mn^{3+} and Mn^{4+} cations [67] also increases. This is reflected in the changes in the Curie–Weiss temperature.

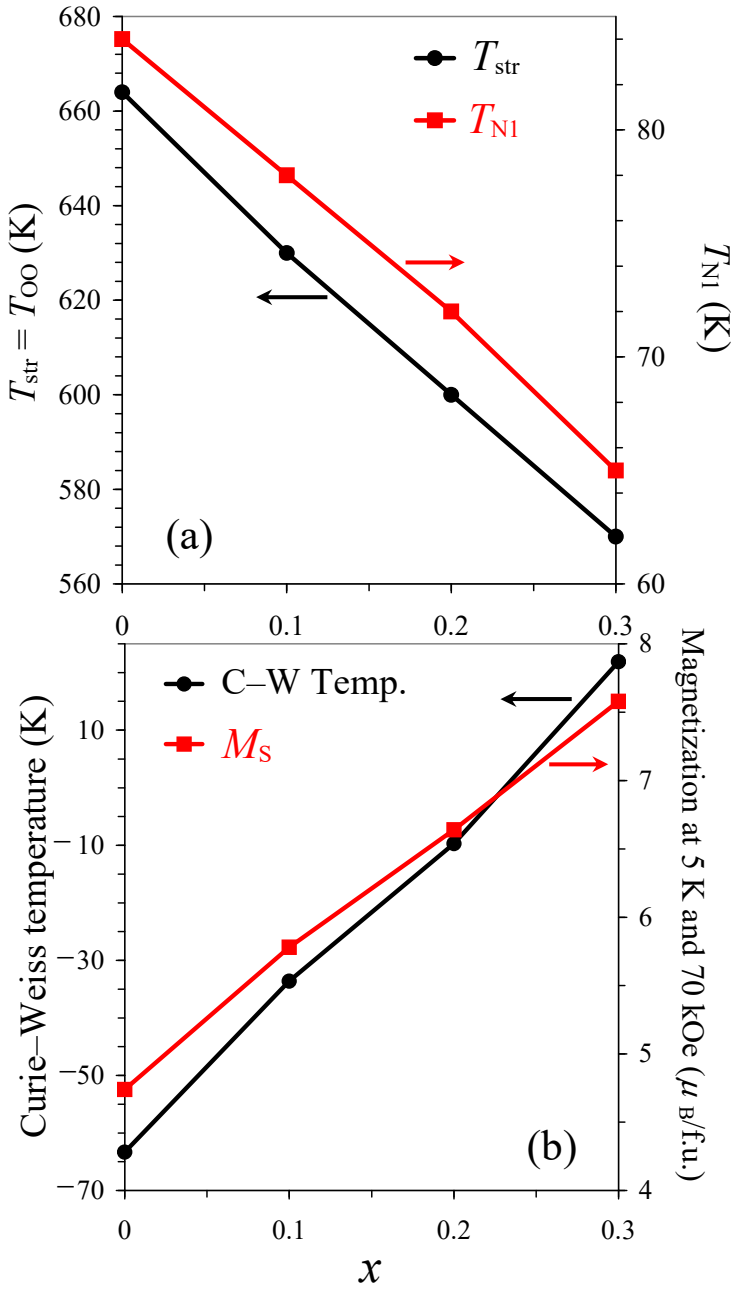

Figure 5. (**a**) Compositional dependence of the structural transition temperature ($T_{srt} = T_{OO}$; black, the left-hand axis) and the first magnetic transition temperature (T_{N1}; red, the right-hand axis) in the $NdCu_xMn_{7-x}O_{12}$ solid solutions. (**b**) Compositional dependence of the Curie–Weiss temperature (black, the left-hand axis) and the magnetization values (at T = 5 K and H = 70 kOe) (red, the right-hand axis).

Isothermal magnetization curves (M versus H) at T = 5 K are given on Figure 6. These are typical for ferrimagnets with well-defined hysteresis near the origin and gradual continuous increases in magnetization at higher magnetic fields due to the AFM B sublattice. There were monotonic increases in the remnant magnetization and coercive fields with x and a nearly linear increase in the magnetization values, M_S (at T = 5 K and H = 70 kOe), with x (Figure 5b). Some parameters of the M versus H curves are summarized in Table 1.

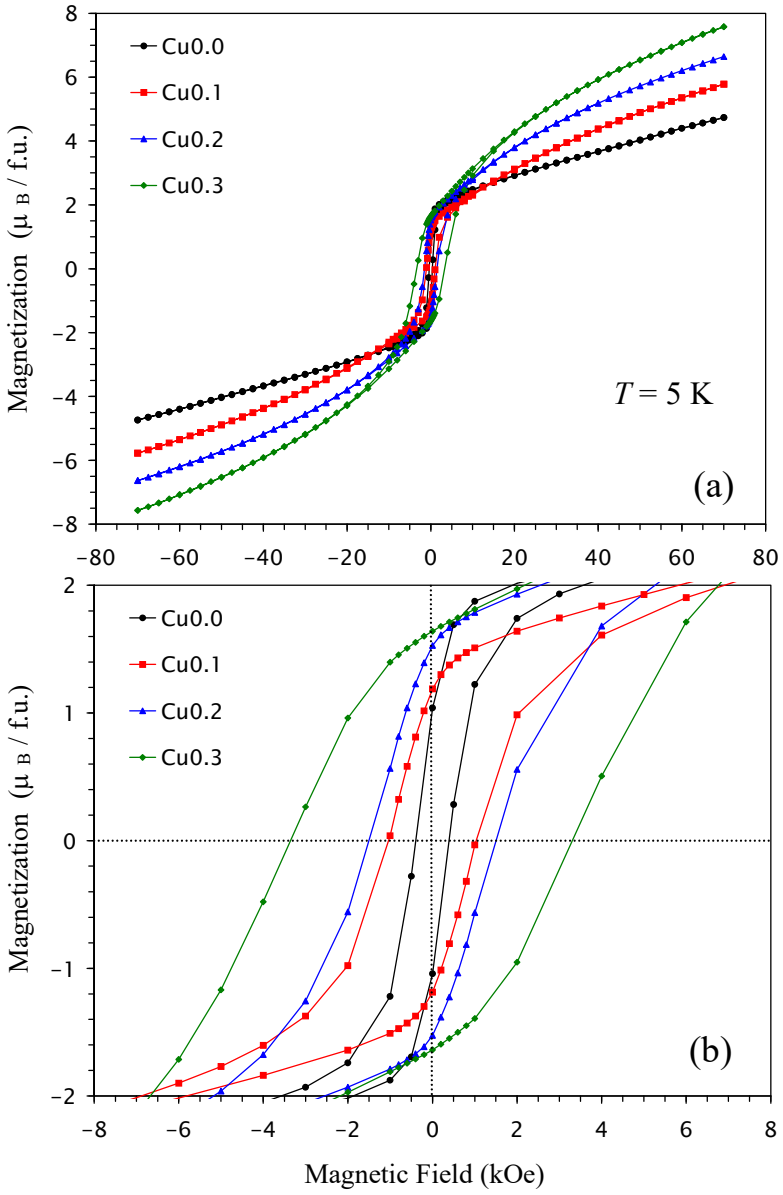

Figure 6. (**a**) *M* versus *H* curves of $NdCu_xMn_{7-x}O_{12}$ with x = 0 (black), 0.1 (red), 0.2 (blue), and 0.3 (green), measured at T = 5 K. (**b**) The same *M* versus *H* curves zoomed in on near the origin.

The results of the specific heat measurements of $NdCu_xMn_{7-x}O_{12}$ with x = 0, 0.1, 0.2, and 0.3 at different magnetic fields are shown in Figure 7. In agreement with the χ versus T curves, $NdMn_7O_{12}$ showed two sharp anomalies at T_{N2} = 12 K and T_{N1} = 84 K and a shoulder-like anomaly at T_{N2} = 9 K (the inset of Figure 7a). The double-peak anomalies near 10–15 K survived in $NdMn_7O_{12}$ at H = 90 kOe. The specific heat anomaly near T_{N2} = 10 K was significantly suppressed in $NdCu_{0.1}Mn_{6.9}O_{12}$ (Figure 7b) and was completely suppressed in $NdCu_{0.2}Mn_{6.8}O_{12}$ (Figure 7c) and $NdCu_{0.3}Mn_{6.7}O_{12}$ (Figure 7d). On the other hand, the magnetic entropy that was released near T_{N2} in $NdMn_7O_{12}$ and $NdCu_{0.1}Mn_{6.9}O_{12}$ moved to higher temperatures (up to about 45 K) in $NdCu_{0.2}Mn_{6.8}O_{12}$ and $NdCu_{0.3}Mn_{6.7}O_{12}$ (the inset of Figure 7d). The C_p/T values of $NdCu_{0.2}Mn_{6.8}O_{12}$ and $NdCu_{0.3}Mn_{6.7}O_{12}$ were nearly the same between 2 K and 60 K.

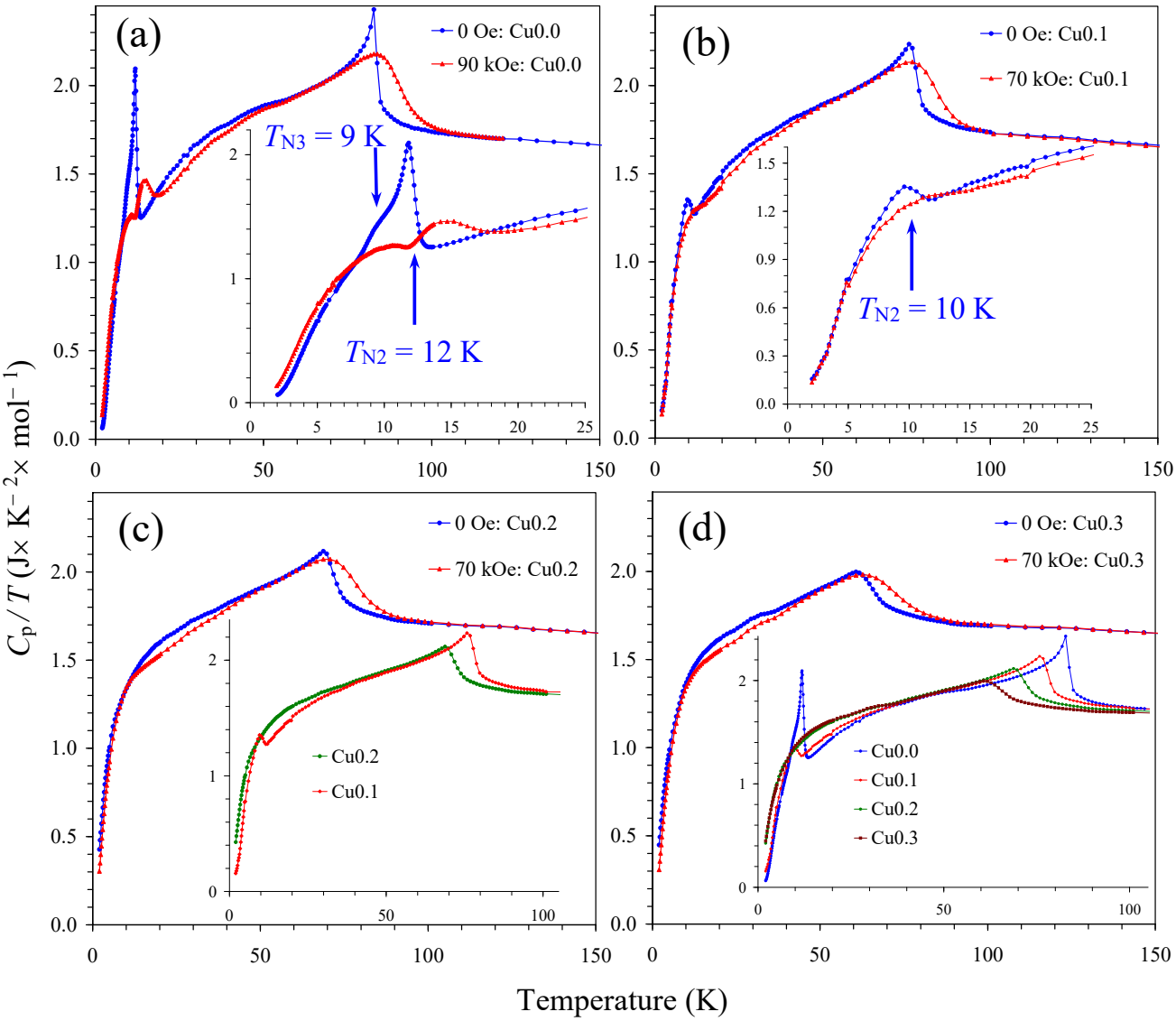

Figure 7. C_p/T versus T curves of the $NdCu_xMn_{7-x}O_{12}$ solid solutions measured at H = 0 Oe (blue curves) and 90 kOe (or 70 kOe) (red curves) during cooling for (**a**) x = 0, (**b**) x = 0.1, (**c**) x = 0.2, and (**d**) x = 0.3. The insets on panels (**a**,**b**) show the same curves below 25 K. Arrows give the magnetic transition temperatures. The inset on panel (**c**) compares C_p/T versus T curves at H = 0 Oe for x = 0.1 and x = 0.2. The inset on panel (**d**) compares C_p/T versus T curves at H = 0 Oe for all samples.

2.2. High-Temperature Structural Transitions

The high-temperature behavior of $NdCu_xMn_{7-x}O_{12}$ with x = 0, 0.1, 0.2, and 0.3 was investigated with differential scanning calorimetry (DSC). $NdMn_7O_{12}$ showed very sharp and strong DSC anomalies near a structural (str) phase transition with T_{str} = 684 K (defined from peak positions on heating curves) [34]. The phase transition temperature remained nearly the same during cycling (three runs) (Figure 8a,b). This structural transition corresponds to the symmetry change from $I2/m$ (below T_{str}) to Im-3 (above T_{str}) and is related to the orbital order (OO) of Mn^{3+} cations at the B sites below T_{str} [12,34].

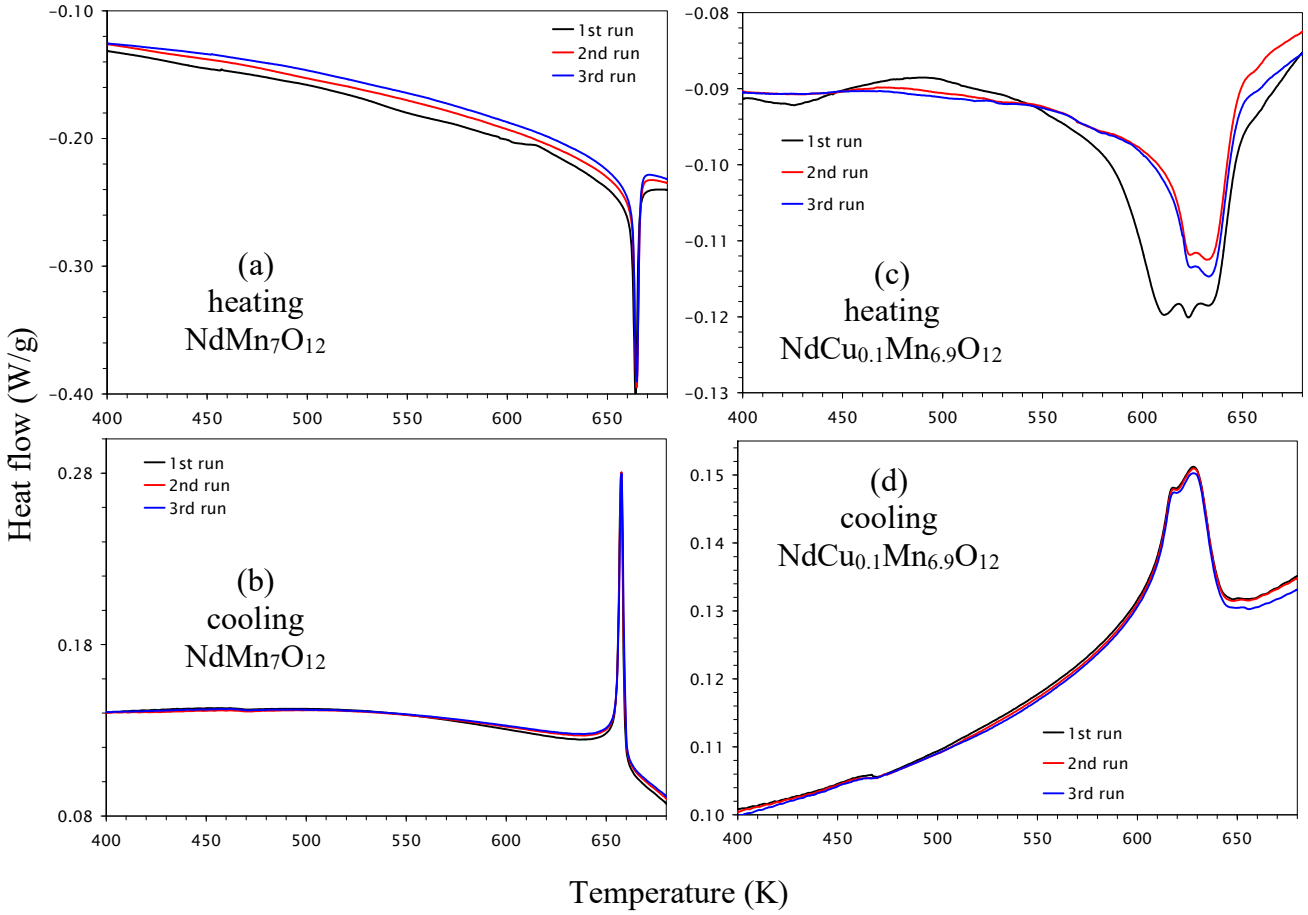

Figure 8. Differential scanning calorimetry (DSC) curves of (**a**,**b**) $NdMn_7O_{12}$ and (**c**,**d**) $NdCu_{0.1}Mn_{6.9}O_{12}$ during (**a**,**c**) heating and (**b**,**d**) cooling, shown between 400 K and 680 K. Three DSC runs are shown. The anomalies near 470 K on the cooling curves are instrumental artifacts.

DSC anomalies were already significantly broadened in $NdCu_{0.1}Mn_{6.9}O_{12}$ (Figure 8c,d), and their intensities were strongly suppressed in comparison with $NdMn_7O_{12}$. In addition, the first heating DSC curve showed three peaks, while the second and third heating DSC curves showed two peaks. The cooling curves were reproducible and showed two peaks. The appearance of two peaks could be explained by the phase separation discussed in the next part. The difference between the first and subsequent DSC heating curves suggests the presence of "annealing" effects, when metastable states, obtained through quenching at a high pressure of 6 GPa, transform to more stable states. The behavior shown in the first and subsequent heating DSC curves was observed, for example, in $BiMn_7O_{12}$ [22].

DSC anomalies became even broader in $NdCu_{0.2}Mn_{6.8}O_{12}$ (Figure 9a,b). There was irreproducibility between the first and subsequent heating curves, while the cooling DSC curves were almost reproducible. In the case of $NdCu_{0.3}Mn_{6.7}O_{12}$, no clear DSC anomalies were observed in the heating curves (Figure 9c), while the cooling curves enabled very broad anomalies starting from about 570 K to be detected (Figure 9d). The structural phase transition temperatures decreased almost linearly with x in the $NdCu_xMn_{7-x}O_{12}$ solid solutions (Figure 5a).

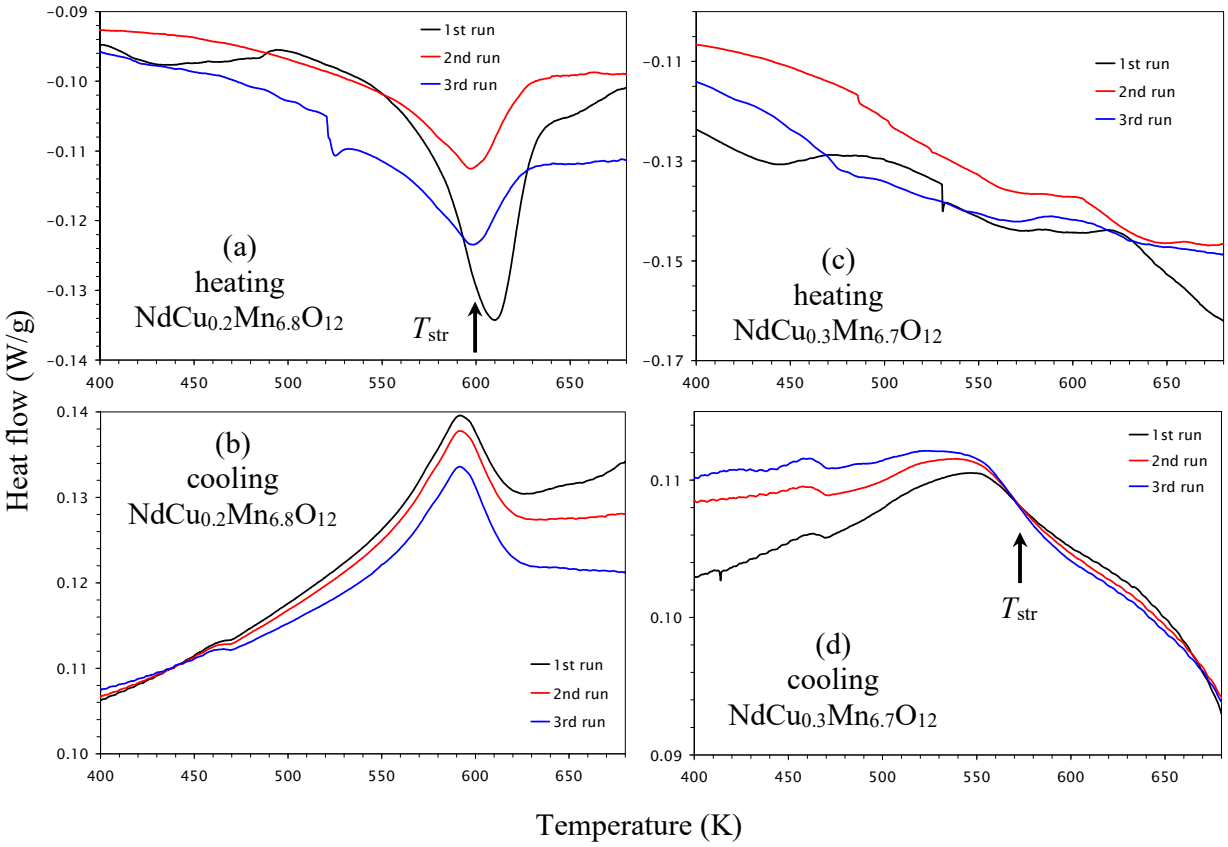

Figure 9. Differential scanning calorimetry (DSC) curves of (**a**,**b**) $NdCu_{0.2}Mn_{6.8}O_{12}$ and (**c**,**d**) $NdCu_{0.3}Mn_{6.7}O_{12}$ during (**a**,**c**) heating and (**b**,**d**) cooling, shown between 400 K and 680 K. Three DSC runs are shown. The anomalies near 470 K on the cooling curves and sharp drops on some of the heating curves are instrumental artifacts.

2.3. Structural Properties

The $NdCu_xMn_{7-x}O_{12}$ samples with x = 0, 0.1, 0.2, and 0.3 did not contain any impurity phases because no impurity peaks could be seen, even for high-resolution, high-intensity synchrotron powder X-ray diffraction (PXRD) data, indicating the high quality of the samples. Reflections on laboratory PXRD data could be readily explained/indexed by assuming the presence of one monoclinic phase with the $I2/m$ symmetry similar to undoped $NdMn_7O_{12}$ [33,34]. However, attempts to fit the synchrotron PXRD data with one $I2/m$ phase were not successful, as one phase could not explain all reflection splitting (see the inset of Figure 10). All attempts to reduce the symmetry (for example, to triclinic symmetry) in a one-phase model were also unsuccessful. On the other hand, all reflection splitting in all samples could be well explained by assuming the presence of two $I2/m$ phases with slightly different lattice parameters (Table S1 in Supplementary Material and Table 2). The DSC results for the x = 0.1 sample (Figure 8c,d) support the conclusion about the presence of two close phases, as each phase can show slightly different T_{str} values. The intensities of the two DSC peaks in the x = 0.1 sample (on the cooling curves and on the second and third heating curves) were comparable with each other, in agreement with the approximate 1:1 ratio of the two monoclinic phases found through synchrotron PXRD. Therefore, in general, the DSC results can provide valuable information about phase separation in the absence of high-resolution synchrotron XRPD data. However, in the x = 0.2 and 0.3 samples, the DSC anomalies became so broad that different T_{str} values were not resolvable.

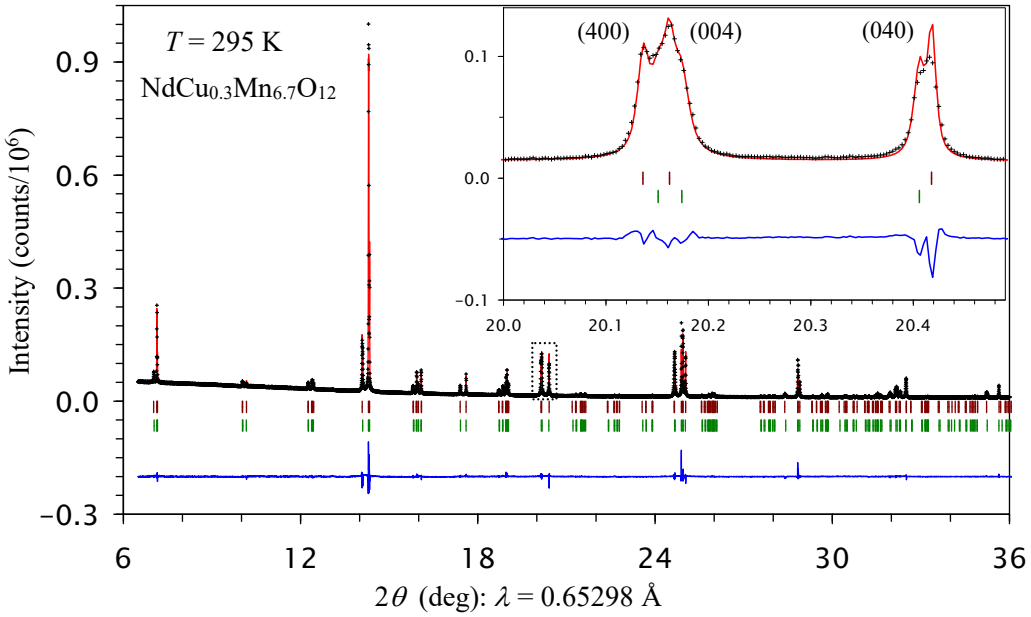

Figure 10. Fragments of the experimental (black crosses), calculated (red line), and difference (blue line at the bottom) room-temperature synchrotron X-ray powder diffraction patterns of $NdCu_{0.3}Mn_{6.7}O_{12}$ in a 2θ range of 6° and 36°, analyzed by the Rietveld method. The tick marks show possible Bragg reflection positions for two $I2/m$ phases. The inset shows a zoomed-in part in a 2θ range of 20.0° and 20.5° (shown by a dotted rectangle in the main panel) and emphasizes the splitting of (400), (004), and (040) reflections from phase separation.

Table 2. Lattice parameters for $NdCu_xMn_{7-x}O_{12}$ with x = 0, 0.1, 0.2, and 0.3 at room temperature (space group $I2/m$), determined from high-resolution synchrotron powder X-ray diffraction. Lattice parameters for two $I2/m$ phases (M1 and M2) are given for x = 0.1, 0.2, and 0.3.

x	Phase	a (Å)	b (Å)	c (Å)	β (°)	V (Å^3)
0	M1	7.49567 (1)	7.35419 (1)	7.49049 (1)	91.2384 (2)	412.814 (1)
0.1	M1	7.48888 (2)	7.35795 (2)	7.48042 (3)	91.1644 (3)	412.107 (2)
	M2	7.48677 (3)	7.35966 (3)	7.47774 (3)	91.1437 (2)	411.942 (3)
0.2	M1	7.48026 (3)	7.36286 (2)	7.47075 (3)	91.0793 (3)	411.387 (2)
	M2	7.47672 (2)	7.36561 (2)	7.46712 (2)	91.0440 (2)	411.151 (2)
0.3	M1	7.47143 (2)	7.36828 (2)	7.46210 (2)	90.9929 (3)	410.739 (2)
	M2	7.46596 (3)	7.37257 (3)	7.45756 (3)	90.9328 (4)	410.434 (3)

Figure 11a shows the compositional dependence of the monoclinic lattice parameters of $NdCu_xMn_{7-x}O_{12}$ with x = 0.1, 0.2, and 0.3. In all cases, the second $I2/m$ phase had a smaller monoclinic distortion in comparison with the first $I2/m$ phase in the sense that the monoclinic β angle (of the second $I2/m$ phase) was closer to 90°, and the difference between the lattice parameters ($a_M - b_M$ and $c_M - b_M$) was smaller for the second $I2/m$ phase. In addition, systematic increases in the splitting of the lattice parameters between the second and first $I2/m$ phases were observed with an increasing x value (Figure 11b). Such monotonic changes in the divergence between the two monoclinic phases provide indirect support that the observed phase separation is an intrinsic property of the $NdCu_xMn_{7-x}O_{12}$ system in the compositional range of x = 0.1–0.3. We found that in the compositional range of x = 0.5–0.8, the $NdCu_xMn_{7-x}O_{12}$ solid solutions (prepared in the same conditions as the x = 0.1–0.3 samples) had the R-3 symmetry and showed no evidence of phase separation (including the DSC results where only one DSC peak was found and high-resolution synchrotron PXRD). The $NdCu_xMn_{7-x}O_{12}$ solid solutions crystallized in the cubic Im-3 structure for x = 1.1–3.0, and we did not see any evidence of phase separation in

the high-resolution synchrotron PXRD; no phase separation was also found in the literature in this compositional range [50,51,54]. Therefore, the phase separation phenomenon depends on the chemical composition/symmetry and is not an artifact of the preparation conditions, mixing procedures, or other factors. The real reason for the phase separation in the 0.1–0.3 samples is not clear and will require additional studies in the future. Magnetic properties were not affected by phase separation, and magnetic measurements could not provide any evidence of phase separation, likely because the magnetic transition temperatures of the two monoclinic phases were too close to each other and all magnetic and specific heat anomalies from the two phases severely overlapped. Monoclinic phases with different lattice parameters were observed in the $A^{3+}Mn_7O_{12}$ systems when the oxygen content was varied (for A = Pr [28]) or small amounts of Mn^{4+} cations were introduced through A-site deficiency (for A = Bi [23,24]). Therefore, one of the driving forces for phase separation in the $NdCu_xMn_{7-x}O_{12}$ solid solutions could be small variations in the oxygen content of the two monoclinic phases. However, the Mn^{3+}/Mn^{4+} distribution and ratio (which depend on the oxygen content and Cu^{2+} doping levels) or lattice strain could also contribute to the phase separation. We also note that phase separation was reported in cubic $CdCu_3Mn_4O_{12}$ [45], prepared under high-pressure conditions; however, in this case, the formation of a CuO impurity (and compositional shifts) could have contributed to the effect. Phase separation was also observed in some of the cubic $CaCu_3Ti_4O_{12}$ samples [68], prepared at ambient pressure.

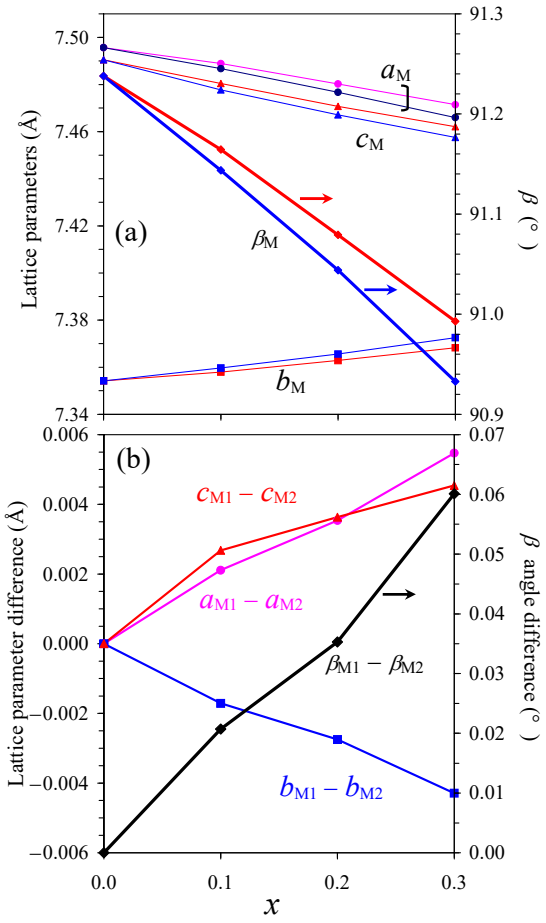

Figure 11. (**a**) Compositional dependence of the monoclinic (M) lattice parameters (the left-hand axis) and monoclinic β angle (the right-hand axis) in $NdCu_xMn_{7-x}O_{12}$ with x = 0, 0.1, 0.2, and 0.3. The lattice parameters of the first $I2/m$ phase (M1) are shown in red and pink, and the lattice parameters of the second $I2/m$ phase (M2) are shown in blue and navy. (**b**) Compositional dependence of the difference in the lattice parameters between phases M1 and M2.

3. Materials and Methods

$NdCu_xMn_{7-x}O_{12}$ samples with x = 0, 0.1, 0.2, and 0.3 were prepared from stoichiometric mixtures of Nd_2O_3 (Rare Metallic Co., Tokyo, Japan, 99.9%), CuO (Rare Metallic Co., Tokyo, Japan, 99.9%), MnO_2 (Alfa Aesar, Ward Hill, MA, USA, 99.99%), and Mn_2O_3. Single-phase Mn_2O_3 was prepared from a commercial MnO_2 chemical (Rare Metallic Co., Tokyo, Japan, 99.99%) by annealing in air at 923 K for 24 h. The synthesis was performed at 6 GPa and 1500 K for 2 h in sealed Au capsules using a belt-type, high-pressure HP instrument. After annealing at 1500 K, the samples were cooled down to room temperature (RT) by turning off the heating current, and the pressure was slowly released.

Powder X-ray diffraction (XRPD) data were collected at RT on a MiniFlex600 diffractometer (Rigaku, Tokyo, Japan) using CuKα radiation (a 2θ range of 5–100°, a step width of 0.02°, and a scan speed of 2 °/min). RT synchrotron XRPD data were measured on the BL15XU beamline (the former NIMS beamline) of SPring-8 [69] between 3.04° and 59.33° at 0.003° intervals in 2θ with a wavelength of λ = 0.65298 Å. The samples were placed into open Lindemann glass capillary tubes (inner diameter: 0.1 mm), which were rotated during the measurements. The Rietveld analysis of all XRPD data and indexing were performed using the RIETAN-2000 program [70].

Magnetic measurements were performed on an SQUID magnetometer (Quantum Design MPMS-XL-7T, San Diego, CA, USA) between 2 K and 350 K in applied fields of 100 Oe and 10 kOe under both zero-field-cooled (ZFC) and field-cooled on cooling (FCC) conditions. Magnetic field dependence was measured at T = 5 K between −70 and 70 kOe. The base temperature of the MPMS-XL-7T magnetometer was 10 K, meaning that samples were inserted slowly into 10 K, and samples moved through a magnet (with finite trapped magnetic fields) below their ordering temperatures. This procedure could be the reason for negative initial magnetization in some ZFC curves (at H = 100 Oe), even though the magnet reset procedure was applied before each ZFC measurement.

Specific heat, C_p, was measured during cooling from 300 K to 2 K at a magnetic field of zero and from 150 K to 2 K at different magnetic fields through a pulse relaxation method using a commercial calorimeter (Quantum Design PPMS, San Diego, CA, USA). All magnetic and specific heat measurements were performed using pieces of pellets.

Differential scanning calorimetry (DSC) curves of powder samples were recorded on a Mettler Toledo DSC1 STAR^e system (Columbus, OH, USA) between 297 K and 703 K in open Al capsules with a heating/cooling rate of 10 K/min. Three DSC runs were performed to check the reproducibility.

4. Conclusions

Solid solutions of $NdCu_xMn_{7-x}O_{12}$ with x = 0, 0.1, 0.2, and 0.3 were synthesized by a high-pressure, high-temperature method at 6 GPa and 1500 K. The specific heat and magnetic measurements uncovered three magnetic transitions at x = 0 (at T_{N3} = 9 K, T_{N2} = 12 K, and T_{N1} = 84 K), two transitions at x = 0.1 (at T_{N2} = 10 K and T_{N1} = 78 K), and only one transition at x = 0.2 (at T_{N1} = 72 K) and x = 0.3 (at T_{N1} = 65 K). The DSC measurements showed sharp and strong peaks near T_{OO} = 664 K at x = 0, while the DSC anomalies were significantly broadened and their intensities were significantly reduced in other samples. Structural transitions were detected near T_{OO} = 630 K at x = 0.1, T_{OO} = 600 K at x = 0.2, and T_{OO} = 570 K at x = 0.3. The first magnetic transition temperature, the Curie–Weiss temperature, the structural transition temperature, and magnetization (at 5 K and 70 kOe) changed almost linearly with x. In addition, the Curie–Weiss temperature changed from negative (for x = 0, 0.1, and 0.2) to positive (for x = 0.3). The high-resolution synchrotron powder X-ray diffraction and DSC studies provided strong evidence that a phase separa-

tion phenomenon took place in the x = 0.1–0.3 samples, where two $I2/m$ phases with an approximate ratio of 1:1 were present.

Supplementary Materials: The following supporting information can be downloaded at https://www.mdpi.com/article/10.3390/molecules30234561/s1: Table S1: Structure parameters of two monoclinic phases in $NdCu_{0.3}Mn_{6.7}O_{12}$.

Author Contributions: Conceptualization, A.A.B.; methodology, A.A.B.; validation, A.A.B.; formal analysis, A.A.B.; investigation, A.A.B., R.L. and K.Y.; resources, K.Y.; data curation, A.A.B.; writing—original draft preparation, A.A.B.; writing—review and editing, A.A.B.; supervision, A.A.B. and K.Y.; project administration, A.A.B.; funding acquisition, K.Y. All authors have read and agreed to the published version of the manuscript.

Funding: This work was partially supported by a Grant-in-Aid for Scientific Research (No. JP25K01657) from the Japan Society for the Promotion of Science.

Institutional Review Board Statement: Not applicable.

Data Availability Statement: The raw data supporting the conclusions of this article will be made available by the author on request.

Acknowledgments: The synchrotron radiation experiments were conducted at the former NIMS beamline (BL15XU) of SPring-8 with the approval of the former NIMS Synchrotron X-ray Station (proposal number: 2020A4501). We thank M. Tanaka and Y. Katsuya for their help at SPring-8. MANA was supported by the World Premier International Research Center Initiative (WPI), MEXT, Japan.

Conflicts of Interest: The authors declare no conflicts of interest.

References

1. Mitchell, R.H. *Perovskites: Modern and Ancient*; Almaz Press: Thunder Bay, ON, Canada, 2002.
2. Abakumov, A.M.; Tsirlin, A.A.; Antipov, E.V. Transition-metal perovskites. In *Comprehensive Inorganic Chemistry II: From Elements to Applications*, 2nd ed.; Reedijk, J., Poeppelmeier, K.R., Eds.; Elsevier: Amsterdam, The Netherlands, 2013; Volume 2, pp. 1–40.
3. Knapp, M.C.; Woodward, P.M. A-site cation ordering in $AA'BB'O_6$ perovskites. *J. Solid State Chem.* **2006**, *179*, 1076–1085. [CrossRef]
4. King, G.; Woodward, P.M. Cation ordering in perovskites. *J. Mater. Chem.* **2010**, *20*, 5785–5796. [CrossRef]
5. Vasala, S.; Karppinen, M. $A_2B'B''O_6$ perovskites: A review. *Prog. Solid State Chem.* **2015**, *43*, 1–36. [CrossRef]
6. Glazer, A.M. Simple ways of determining perovskite structures. *Acta Cryst.* **1975**, *A31*, 756–762. [CrossRef]
7. Bochu, B.; Chenavas, J.; Joubert, J.C.; Marezio, M. High pressure synthesis and crystal structure of a new series of perovskite-like compounds CMn_7O_{12} (C = Na, Ca, Cd, Sr, La, Nd). *J. Solid State Chem.* **1974**, *11*, 88–93. [CrossRef]
8. Vasil'ev, A.N.; Volkova, O.S. New functional materials $AC_3B_4O_{12}$ (Review). *Low Temp. Phys.* **2007**, *33*, 895–914. [CrossRef]
9. Long, Y. A-site ordered quadruple perovskite oxides $AA'_3B_4O_{12}$. *Chin. Phys. B* **2016**, *25*, 078108. [CrossRef]
10. Yamada, I. Novel catalytic properties of quadruple perovskites. *Sci. Technol. Adv. Mater.* **2017**, *18*, 541–548. [CrossRef]
11. Ding, J.; Zhu, X.H. Research progress on quadruple perovskite oxides. *J. Mater. Chem. C* **2024**, *12*, 9510–9561. [CrossRef]
12. Belik, A.A.; Johnson, R.D.; Khalyavin, D.D. The rich physics of A-site-ordered quadruple perovskite manganites AMn_7O_{12}. *Dalton Trans.* **2021**, *50*, 15458–15472. [CrossRef]
13. Belik, A.A. Rise of A-site columnar-ordered $A_2A'A''B_4O_{12}$ quadruple perovskites with intrinsic triple order. *Dalton Trans.* **2018**, *47*, 3209–3217. [CrossRef]
14. Prodi, A.; Gilioli, E.; Gauzzi, A.; Licci, F.; Marezio, M.; Bolzoni, F.; Huang, Q.; Santoro, A.; Lynn, J.W. Charge orbital and spin ordering phenomena in the mixed valence manganite $(NaMn^{3+}{}_3)(Mn^{3+}{}_2Mn^{4+}{}_2)O_{12}$. *Nat. Mater.* **2004**, *3*, 48–52. [CrossRef]
15. Prodi, A.; Daoud-Aladine, A.; Gozzo, F.; Schmitt, B.; Lebedev, O.; van Tendeloo, G.; Gilioli, E.; Bolzoni, F.; Aruga-Katori, H.; Takagi, H.; et al. Commensurate structural modulation in the charge- and orbitally ordered phase of the quadruple perovskite $(NaMn_3)Mn_4O_{12}$. *Phys. Rev. B* **2014**, *90*, 180101. [CrossRef]
16. Johnson, R.D.; Chapon, L.C.; Khalyavin, D.D.; Manuel, P.; Radaelli, P.G.; Martin, C. Giant improper ferroelectricity in the ferroaxial magnet $CaMn_7O_{12}$. *Phys. Rev. Lett.* **2012**, *108*, 067201. [CrossRef] [PubMed]
17. Imamura, N.; Karppinen, M.; Motohashi, T.; Fu, D.; Itoh, M.; Yamauchi, H. Positive and negative magnetodielectric effects in A-site ordered $(BiMn_3)Mn_4O_{12}$ perovskite. *J. Am. Chem. Soc.* **2008**, *130*, 14948–14949. [CrossRef]

18. Behr, D.; Belik, A.A.; Khalyavin, D.D.; Johnson, R.D. $BiMn_7O_{12}$: Polar antiferromagnetism by inverse exchange striction. *Phys. Rev. B* **2023**, *107*, L140402. [CrossRef]
19. Gauzzi, A.; Rousse, G.; Mezzadri, F.; Calestani, G.L.; Andre, G.; Bouree, F.; Calicchio, M.; Gilioli, E.; Cabassi, R.; Bolzoni, F.; et al. Magnetoelectric coupling driven by inverse magnetostriction in multiferroic $BiMn_3Mn_4O_{12}$. *J. Appl. Phys.* **2013**, *113*, 043920. [CrossRef]
20. Mezzadri, F.; Calestani, G.; Calicchio, M.; Gilioli, E.; Bolzoni, F.; Cabassi, R.; Marezio, M.; Migliori, A. Synthesis and characterization of multiferroic $BiMn_7O_{12}$. *Phys. Rev. B* **2009**, *79*, 100106. [CrossRef]
21. Slawinski, W.A.; Okamoto, H.; Fjellvag, H. Triclinic crystal structure distortion of multiferroic $BiMn_7O_{12}$. *Acta Crystallogr. Sect. B Struct. Sci. Cryst. Eng. Mater.* **2017**, *73*, 313–320. [CrossRef]
22. Belik, A.A.; Matsushita, Y.; Kumagai, Y.; Katsuya, Y.; Tanaka, M.; Stefanovich, S.Y.; Lazoryak, B.I.; Oba, F.; Yamaura, K. Complex structural behavior of $BiMn_7O_{12}$ quadruple perovskite. *Inorg. Chem.* **2017**, *56*, 12272–12281. [CrossRef]
23. Imamura, N.; Karppinen, M.; Yamauchi, H. Synthesis and properties of monoclinic and cubic forms of the A-site-ordered $(BiMn_3)Mn_4O_{12}$ perovskite. *Chem. Mater.* **2009**, *21*, 2179–2183. [CrossRef]
24. Mezzadri, F.; Buzzi, M.; Pernechele, C.; Calestani, G.; Solzi, M.; Migliori, A.; Gilioli, E. Polymorphism and multiferroicity in $Bi_{1-x/3}(Mn^{III}{}_3)(Mn^{III}{}_{4-x}Mn^{IV}{}_x)O_{12}$. *Chem. Mater.* **2011**, *23*, 3628–3635. [CrossRef]
25. Okamoto, H.; Imamura, N.; Karppinen, M.; Yamauchi, H.; Fjellvag, H. Crystal structure of the monoclinic and cubic polymorphs of $BiMn_7O_{12}$. *J. Solid State Chem.* **2010**, *183*, 186–191. [CrossRef]
26. Verseils, M.; Mezzadri, F.; Delmonte, D.; Baptiste, B.; Klein, Y.; Shcheka, S.; Chapon, L.C.; Hansen, T.; Gilioli, E.; Gauzzi, A. Effect of chemical pressure induced by La^{3+}/Y^{3+} substitution on the magnetic ordering of $(AMn_3)Mn_4O_{12}$ quadruple perovskites. *Phys. Rev. Mater.* **2017**, *1*, 064407. [CrossRef]
27. Verseils, M.; Mezzadri, F.; Delmonte, D.; Cabassi, R.; Baptiste, B.; Klein, Y.; Calestani, G.; Bolzoni, F.; Gilioli, E.; Gauzzi, A. Centrosymmetry breaking and ferroelectricity driven by short-range magnetic order in the quadruple perovskite $(YMn_3)Mn_4O_{12}$. *Inorg. Chem.* **2019**, *58*, 14204–14211. [CrossRef] [PubMed]
28. Mezzadri, F.; Calicchio, M.; Gilioli, E.; Cabassi, R.; Bolzoni, F.; Calestani, G.; Bissoli, F. High-pressure synthesis and characterization of $PrMn_7O_{12}$ polymorphs. *Phys. Rev. B* **2009**, *79*, 014420. [CrossRef]
29. Cabassi, R.; Bolzoni, F.; Gilioli, E.; Bissoli, F.; Prodi, A.; Gauzzi, A. Jahn-Teller-induced crossover of the paramagnetic response in the singly valent eg system $LaMn_7O_{12}$. *Phys. Rev. B* **2010**, *81*, 214412. [CrossRef]
30. Okamoto, H.; Karppinen, M.; Yamauchi, H.; Fjellvag, H. High temperature synchrotron X-ray diffraction study of $LaMn_7O_{12}$. *Solid State Sci.* **2009**, *11*, 1211–1215. [CrossRef]
31. Prodi, A.; Gilioli, E.; Cabassi, R.; Bolzoni, F.; Licci, F.; Huang, Q.; Lynn, J.W.; Affronte, M.; Gauzzi, A.; Marezio, M. Magnetic structure of the high-density single-valent eg Jahn-Teller system $LaMn_7O_{12}$. *Phys. Rev. B* **2009**, *79*, 085105. [CrossRef]
32. Zhang, L.; Terada, N.; Johnson, R.D.; Khalyavin, D.D.; Manuel, P.; Katsuya, Y.; Tanaka, M.; Matsushita, Y.; Yamaura, K.; Belik, A.A. High-pressure synthesis, structures, and properties of trivalent A-site-ordered quadruple perovskites RMn_7O_{12} (R = Sm, Eu, Gd, and Tb). *Inorg. Chem.* **2018**, *57*, 5987–5998. [CrossRef]
33. Johnson, R.D.; Khalyavin, D.D.; Manuel, P.; Zhang, L.; Yamaura, K.; Belik, A.A. Magnetic structures of the rare-earth quadruple perovskite manganites RMn_7O_{12}. *Phys. Rev. B* **2018**, *98*, 104423. [CrossRef]
34. Belik, A.A.; Liu, R.; Zhang, L.; Terada, N.; Tanaka, M.; Yamaura, K. Multiple magnetic transitions and complex magnetic behaviour of the perovskite manganite $NdMn_7O_{12}$. *J. Solid State Chem.* **2022**, *309*, 122969. [CrossRef]
35. Johnson, R.D.; Mezzadri, F.; Manuel, P.; Khalyavin, D.D.; Gilioli, E.; Radaelli, P.G. Evolution of magneto-orbital order upon B-site electron doping in $Na_{1-x}Ca_xMn_7O_{12}$ quadruple perovskite manganites. *Phys. Rev. Lett.* **2018**, *120*, 257202. [CrossRef]
36. Chen, W.-T.; Wang, C.-W.; Cheng, C.-C.; Chuang, Y.-C.; Simonov, A.; Bristowe, N.C.; Senn, M.S. Striping of orbital-order with charge-disorder in optimally doped manganites. *Nat. Comm.* **2021**, *12*, 6319. [CrossRef]
37. Tragheim, B.R.M.; Simpson, S.; Liu, E.P.; Senn, M.S.; Chen, W.-T. Intrinsic electronic phase separation and competition between G-type, C-type, and CE-type charge and orbital ordering modes in $Hg_{1-x}Na_xMn_3Mn_4O_{12}$. *Phys. Rev. B* **2024**, *110*, 245123. [CrossRef]
38. Chenavas, J.; Joubert, M.; Marezio, J.C.; Bochu, B. The synthesis and crystal structure of $CaCu_3Mn_4O_{12}$: A new ferromagnetic-perovskite-like compound. *J. Solid State Chem.* **1975**, *14*, 25–32. [CrossRef]
39. Zeng, Z.; Greenblatt, M.; Subramanian, M.A.; Croft, M. Large low-field magnetoresistance in perovskite-type $CaCu_3Mn_4O_{12}$ without double exchange. *Phys. Rev. Lett.* **1999**, *82*, 3164–3167. [CrossRef]
40. Zhang, Q.; Bréard, Y.; Guillou, F.; Hardy, V. Investigation of the magnetocaloric effect in double distorted perovskites $Ca(Cu_{3-x}Mn_x)Mn_4O_{12}$ ($1 \leq x \leq 2$): From standard ferrimagnetism to glassy ferrimagnetism. *Phys. Rev. B* **2011**, *84*, 224430. [CrossRef]
41. Sánchez-Benítez, J.; Prieto, C.; de Andrés, A.; Alonso, J.A.; Martínez-Lope, M.J.; Casais, M.T. Evidence of two different states in $CaCu_3Mn_4O_{12}$ derivatives with colossal magnetoresistance. *Phys. Rev. B* **2004**, *70*, 024419. [CrossRef]

42. Volkova, O.; Goodilin, E.; Vasiliev, A.; Khomskii, D.; Tristan, N.; Kerschl, P.; Skourski, Y.; Mueller, K.-H.; Buechner, B. $CaCuMn_6O_{12}$ vs. $CaCu_2Mn_5O_{12}$: A comparative study. *J. Exp. Theor. Phys. Lett.* **2005**, *82*, 642–645. [CrossRef]
43. Zeng, Z.; Greenblatt, M.; Sunstrom, J.E.; Croft, M.; Khalid, S. Giant magnetoresistance in $CaCu_3Mn_4O_{12}$-based oxides with perovskite-type structure. *J. Solid State Chem.* **1999**, *147*, 185–198. [CrossRef]
44. Sánchez-Benítez, J.; Alonso, J.A.; Martínez-Lope, M.J.; Casais, M.T.; Martínez, J.L.; de Andrés, A.; Fernández-Díaz, M.T. Preparation, crystal and magnetic structure, and magnetotransport properties of the double perovskite $CaCu_{2.5}Mn_{4.5}O_{12}$. *Chem. Mater.* **2003**, *15*, 2193–2200. [CrossRef]
45. Sánchez-Benítez, J.; Kayser, P.; Morales-García, Á.; Martínez-Lope, M.J.; Mompeán, F.J.; Xu, J.; Jin, Z.; Alonso, J.A. Preparation, crystal structure, and magnetotransport properties of the new $CdCu_3Mn_4O_{12}$ perovskite: A comparison with density functional theory calculations. *J. Phys. Chem. C* **2014**, *118*, 9652–9658. [CrossRef]
46. Samaras, D.; Bochu, B.; Joubert, J.C. Synthesis, composition, and magnetic properties of the ferrimagnetic $NdCu_{3-x}Mn_{4+x}O_{12}$ perovskite-like phases. *J. Solid State Chem.* **1984**, *53*, 323–328. [CrossRef]
47. Sánchez-Benítez, J.; Alonso, J.A.; Falcón, H.; Martínez-Lope, M.J.; de Andrés, A.; Fernández-Díaz, M.T. Preparation under high pressures and neutron diffraction study of new ferromagnetic $RCu_3Mn_4O_{12}$ (R = Pr, Sm, Eu, Gd, Dy, Ho, Tm, Yb) perovskites. *J. Phys. Condens. Matter.* **2005**, *17*, S3063. [CrossRef]
48. Zhang, W.; Yao, L.D.; Yang, L.X.; Liu, Z.X.; Jin, C.Q.; Yu, R.C. Charge ordering in $PrCuMn_6O_{12}$ and its behavior under pressure. *J. Appl. Phys.* **2010**, *107*, 023914. [CrossRef]
49. Sanchez-Benitez, J.; Alonso, J.A.; de Andres, A.; Martinez-Lope, M.J.; Martinez, J.L.; Munoz, A. Peculiar magnetic behavior of the $TbCu_3Mn_4O_{12}$ complex perovskite. *Chem. Mater.* **2005**, *17*, 5070–5076. [CrossRef]
50. Zhang, Q.; Bréard, Y.; Hardy, V. Spin-glass-like state and reversible room-temperature magnetocaloric effect in double distorted perovskites $Nd(Cu_{3-x}Mn_x)Mn_4O_{12}$. *Inorg. Chem.* **2022**, *61*, 5792–5799. [CrossRef]
51. Retuerto, M.; Martínez-Lope, M.J.; Sánchez-Benítez, J.; García-Hernández, M.; Fernández-Díaz, M.T.; Alonso, J.A. Synthesis, magnetic properties, and neutron diffraction study of the complex perovskites $R(Cu_{3-x}Mn_x)Mn_4O_{12}$ (R = Pr, Nd and x = 1, 2). *J. Appl. Phys.* **2010**, *108*, 083905. [CrossRef]
52. Alonso, J.A.; Sánchez-Benítez, J.; de Andrés, A.; Martínez-Lope, M.J.; Casais, M.T.; Martínez, J.L. Enhanced magnetoresistance in the complex perovskite $LaCu_3Mn_4O_{12}$. *Appl. Phys. Lett.* **2003**, *83*, 2623–2625. [CrossRef]
53. Muñoz, A.; Martínez-Lope, M.J.; Retuerto, M.; Falcón, H.; Alonso, J.A. Ferromagnetic behavior in $La(Cu_{3-x}Mn_x)Mn_4O_{12}$ (x = 1, 2) perovskites. *J. Appl. Phys.* **2008**, *104*, 083911. [CrossRef]
54. Sanchez-Benitez, J.; Alonso, J.A.; Martinez-Lope, M.J.; de Andres, A.; Fernandez-Diaz, M.T. Enhancement of the Curie temperature along the perovskite series $RCu_3Mn_4O_{12}$ driven by chemical pressure of R^{3+} cations (R = rare earths). *Inorg. Chem.* **2010**, *49*, 5679–5685. [CrossRef]
55. Sánchez-Benítez, J.; Martínez-Lope, M.J.; Alonso, J.A. Preparation at moderate pressures, crystal and magnetic structure and magnetotransport of the ferrimagnetic $CeCu_3Mn_4O_{12}$ perovskite. *J. Appl. Phys.* **2010**, *107*, 103904. [CrossRef]
56. Khalyavin, D.D.; Johnson, R.D.; Orlandi, F.; Radaelli, P.G.; Manuel, P.; Belik, A.A. Emergent helical texture of electric dipoles. *Science* **2020**, *369*, 680–684. [CrossRef]
57. Zhang, Y.; Xu, M.Y.; Li, J.; Sung, S.H.; Cheong, S.-W.; Xie, W.W.; Baggari, I.E. Mesoscopic helices of polar domains in a quadruple perovskite. *arXiv* **2025**, arXiv:2506.03048v2. [CrossRef]
58. Belik, A.A.; Matsushita, Y.; Khalyavin, D.D. Reentrant structural transitions and collapse of charge and orbital orders in quadruple perovskites. *Angew. Chem. Int. Ed.* **2017**, *56*, 10423. [CrossRef]
59. Belik, A.A.; Matsushita, Y.; Tanaka, M.; Johnson, R.D.; Khalyavin, D.D. A plethora of structural transitions, distortions and modulations in Cu-doped $BiMn_7O_{12}$ quadruple perovskites. *J. Mater. Chem. C* **2021**, *9*, 10232–10242. [CrossRef]
60. Troyanchuk, I.O.; Balyko, L.V.; Bashkirov, L.A. Crystal structure phase transitions in the perovskites $A(Cu_{1-x}Mn_x)Mn_4O_{12}$ ($A = Na^+, Ca^{2+}, Y^{3+}, La^{3+}$). *Cryst. Res. Technol.* **1986**, *21*, 705–710. [CrossRef]
61. Slawinski, W.; Przenioslo, R.; Sosnowska, I.; Bieringer, M.; Margiolaki, I.; Fitch, A.N.; Suard, E. Phase coexistence in $CaCu_xMn_{7-x}O_{12}$ solid solutions. *J. Solid State Chem.* **2006**, *179*, 2443–2451. [CrossRef]
62. Slawinski, W.; Przenioslo, R.; Sosnowska, I.; Bieringer, M.; Margiolaki, I.; Fitch, A.N.; Suard, E. Charge ordering in $CaCu_xMn_{7-x}O12$ (x = 0.0 and 0.1) compounds. *J. Phys. Condens. Matter* **2008**, *20*, 104239. [CrossRef]
63. Slawinski, W.; Przenioslo, R.; Sosnowska, I.; Bieringer, M. Structural and magnetic modulations in $CaCu_xMn_{7-x}O_{12}$. *J. Phys. Condens. Matter* **2010**, *22*, 186001. [CrossRef]
64. Slawinski, W.; Przenioslo, R.; Sosnowska, I.; Petrícek, V. Helical screw type magnetic structure of the multiferroic $CaMn_7O_{12}$ with low Cu-doping. *Acta Crystallogr. Sec. B* **2012**, *68*, 240–249. [CrossRef]
65. Glazkova, I.S.; Rusakov, V.S.; Sobolev, A.V.; Matsnev, M.E.; Gapochka, A.M.; Gubaidulina, T.V.; Presniakov, I.A. Probe Mössbauer diagnostics of charge ordering in manganites $CaCu_xMn_{7-x}O_{12}$ ($0 \leq x \leq 1$). *J. Exp. Theor. Phys.* **2019**, *129*, 1017–1028. [CrossRef]
66. Kittel, C.; McEuen, P. *Introduction to Solid State Physics*; John Wiley & Sons, Inc.: New York, NY, USA, 2005.
67. Coey, J.M.D.; Viret, M.; von Molnar, S. Mixed-valence manganites. *Adv. Phys.* **2009**, *58*, 571–697. [CrossRef]

68. Sławiński, W.; Przeniosło, R.; Wardecki, D.; Sosnowska, I.; Hill, A.; Fitch, A.N.; Bieringer, M. Dilemma on the crystal structure of $CaCu_3Ti_4O_{12}$. *Mater. Res. Express* **2014**, *1*, 016306. [CrossRef]
69. Tanaka, M.; Katsuya, Y.; Matsushita, Y.; Sakata, O. Development of a synchrotron powder diffractometer with a one-dimensional X-ray detector for analysis of advanced materials. *J. Ceram. Soc. Jpn.* **2013**, *121*, 287–290. [CrossRef]
70. Izumi, F.; Ikeda, T. A Rietveld-analysis program RIETAN-98 and its applications to zeolites. *Mater. Sci. Forum* **2000**, *321–324*, 198–205. [CrossRef]